provide information on the effect of jagged vs smooth rocks on the radar return and might contribute to an improved theory of radar scattering by the lunar surface which could then be applied to the radar data from additional unexplored areas.

Tycho Rim: (11.3°W, 40.9°S)
At Tycho, the angle of incidence is large (>50°) and interpretation of the radar maps must be carried out with more caution. As pointed out earlier, the effect of local tilts on the backscattered power at such large angles of incidence has become significant in the depolarized map, and must be separated out from the physical character of the surface itself which is of primary concern here.

From both optical and radar pictures, the area surrounding the proposed landing site is relatively flat, and the radar should give a fairly good idea of the surface structure. The polarized and depolarized values are about 1.4 and/1.8 times the average for this angle of incidence, indicating as expected, that the area is considerably rockier than average. As in the case of the proposed Copernicus landing site, the radar shows that the 2 km × 2 km Tycho site is by far the smoothest for 20 km around. The modal backscatter values elsewhere in the neighborhood are about 2.0 and 2.5 times the corresponding averages.

Marius Hills: (56.6°W, 14.6°N)
There is no bold relief apparent in this area which might have complicated the interpretation of the radar maps at this high angle of incidence. A number of features show up on both polarized and depolarized radar maps, but none are very strong and the general values of backscatter are about average (1.0 to 1.3 times the average for this angle of incidence). The hills do not appear unusually enhanced, and so should be well covered with soil. There are no indications of large-scale rocky protuberances. From the radar measurements the surface somewhat similar to the Apollo 11 and 12 sites, although one must keep in mind that the radar results are not greatly influenced by the chemistry or age of the surface, except indirectly by the state of erosion of surface rocks.

References

Evans, J. V. and Hagfors, T.: 1971, in *Adv. Astron. and Astrophys.*, Academic Press, New York and London, pp. 29–105.
Moore, H. J. and Zisk, S. H.: 1973, 'Calibration of Radar Data from Apollo 17 and Other Mission Results', submitted for *Apollo 17 Preliminary Science Report*, NASA; to be published.
Pettengill, G. H. and Thompson, T. W.: 1968, *Icarus* **8**, 457–471.
Pettengill, G. H., Zisk, S. H., Thompson, T. W.: 1973, *The Moon*, this issue, p. 3.
Pieters, C., McCord, T. B., Zisk, S. H., and Adams, J. B.: 'Lunar Black Spots and the Nature of the Apollo 17 Landing Area', *J. Geophys. Res.*, to be published.
Pollack, J. B. and Whitehill, L.: 1972, *J. Geophys. Res.* **77**, 4289–4303.
Thompson, T. W.: 1973, *The Moon*, this issue, p. 51.
Tyler, G. L.: 1968, *Nature* **219**, 1243–1244.
Zisk, S. H. and Moore, H. J.: 1972, *Apollo 16 Preliminary Science Report*, NASA SP-315, Government Printing Office.
Zisk, S. H., Carr, M. H., Masursky, H., Shorthill, R. W., and Thompson, T. W.: 1971, *Science* **173**, 808–811.

ATLAS OF LUNAR RADAR MAPS AT 70-cm WAVELENGTH*

THOMAS W. THOMPSON
National Astronomy and Ionospheric Center, Arecibo, Puerto Rico
and
Jet Propulsion Laboratory, Pasadena, Calif., U.S.A.

(Received 30 June, 1973)

Abstract. The intensity distribution of lunar radar echoes has been mapped for two-thirds of the earth-visible lunar surface at a wavelength of 70 cm. The depolarizing effects of the lunar surface were observed by simultaneously receiving the radar echoes in opposite polarizations. These echoes were mapped with areal resolutions of 25–100 km². Mappings with this resolution confirmed that the young craters have enhanced returns. A few craters were found to have enhanced echoes only from their rims. Backscattering differences were also observed between various areas within a mare, between different highland areas, and between maria and adjacent highlands. These scattering differences were interpreted with a simple model, which assumed that the surface backscattered with varying amounts of quasi-specular and diffuse power. Only an increase in the diffuse power was needed to give the numerical values of the enhancements.

1. Introduction

This article is the second of a series of four articles describing the radar mapping of the Moon. The first article describes the techniques of measurement, the third article describes the mapping of radar echoes at 3.8 cm wavelength, and the fourth article describes the correlation of these radar mappings with their data sets.

In this paper, radar observations at a wavelength of 70 cm are described. These 70-cm-wavelength observations are a refinement of earlier experiments made in 1964 and reported by Thompson and Dyce (1965). These earlier measurements demonstrated that narrow antenna beams could resolve the delay-Doppler ambiguity in the manner described in the first paper of this series. For the new measurements described here, the surface resolution is 25–100 km², a 20-fold improvement over the 1964 measurements. Furthermore, the mapping was extended to two-thirds of the earth-visible hemisphere and radar echoes were observed in opposite polarizations to measure the depolarization generated by the lunar surface.

The 70 cm wavelength used here is nearly centered in the radar window – the band of frequencies available for earth-based observations. The longest wavelength for Earth observations is several meters because of refractive effects of charged particles

* The radar mapping was performed at the Arecibo Observatory and was supported by NASA Grant NGR-33-010-024. The continuing support of the Arecibo Observatory by the Advanced Research Projects Agency and the National Science Foundation was an invaluable contribution to these mappings. Data display and analysis were performed at the Jet Propulsion Laboratory, California Institute of Technology, which is sponsored by the National Aeronautics and Space Administration, under Contract No. NAS 7-100.

The Moon **10** (1974) 51–85.

in the Earth's ionosphere. The shortest wavelength for Earth observations is a few centimeters because of absorption by water and oxygen molecules in the Earth's atmosphere. Observations at 3.8-cm, which are near this short wavelength limit, are described in the next article of this series.

2. Procedures

For the mapping presented here, radar observatons were carried out at a wavelength of 70 cm at the National Astronomy and Ionospheric Center, Arecibo, Puerto Rico, operated by Cornell University. Typical operating parameters for these observations are given in Table I. The general details of the operating procedures have been described in the first paper in this series, while specific details of the electronics and data processing have been given by Thompson, 1968. Observations were carried out from November 1966 until September 1969.

Because of the refined resolution of this mapping, it was impossible to map the entire lunar surface in a single observation. In particular, constraints imposed by the data processing limited the number of mapped points for a single observation to 6500. With this limitation, the surface area mapped in a single observation was approximately 5×10^5 km^2, which is about 1/50 of the earth-visible lunar surface and nearly

TABLE I

Typical operating parameters for lunar mapping at 70-cm wavelength

Radar and data processing parameters	
Antenna latitude (geodetic), deg	18°20′46″
Antenna longitude, deg	66°45′11″
Antenna gain, dB	~56
Half-power antenna beamwidth, arc sec	7
Antenna configuration	330-m spherical reflector
Radar frequency, MHz	430.0
Radar wavelength, cm	69.8
Peak transmitter power, MW	1.0
Transmitter pulse length, μs	10–40[a]
Pulse repetition frequency, pps	10
Transmitted polarization	Left-hand circular
Received polarizations	Right- and left-hand circular
Background sky temperature on Moon, K	500
Echo sampling period, μs	10–40[a]
Surface range resolution, km	5–10
Coherent processing interval, s	51.2
Spectral sample spacing, Hz	0.02
Limb-limb Doppler spread of Moon, Hz	10–14[a]
Spectra summed per map	25–50[a]
Map elements in range-frequency space	51200 per polarization
Map elements per LAC chart	6561 per polarization
Areal coverage per LAC chart, km^2	5×10^5
Number of LAC charts mapped	44

[a] These quantities varied from map to map within the given limits.

equals the area shown in a single Lunar Chart (LAC). Since these LAC's and radar maps covered nearly equal areas, it was convenient to map the radar echoes from one observation onto a single LAC map.

For these 70-cm observations, the resolution was limited by the frequency analysis. With typical lunar rotation rates and a synthesized spectral bandwidth of 0.02 Hz, the surface resolution was 5–10 km. To obtain the same surface resolution in delay, transmitter pulses and delay sample spacing were between 10 and 40 μs, which is several times the capabilities of the radar. Also, the delay resolution was adjusted from run to run to give the best resolution consistent with the constraint that the delay spread across the mapped area fall within 100 consecutive samples. This number of delay samples was fixed by several subsequent data storage and processing constraints.

Each observation for a single LAC map was done in the manner described in Section D of the previous article. The normalization for average echo strength used an empirical law for observations at a wavelength of 68 cm (see Table I; Hagfors, 1967). It is doubtful whether the small difference between the 68- and 70-cm wavelengths would cause significant scattering differences. Also, this correction for mean scattering was not calibrated, so a direct comparison between difference observations is not possible.

A total of 44 LAC charts were mapped, covering approximately two-thirds of the earth-visible surface. Opposite polarization senses were mapped for each LAC chart. The radar transmitted right-hand circularly polarized waves; echoes in left-hand circular polarization are called polarized (often referred to as expected) and echoes in right-hand circular polarization are called depolarized.

3. Results

Typically, LAC chart radar maps contain 6561 individual values of echo strength for each polarization. Thus, approx 500000 values of echo strength were accumulated for all of the observations. Digital photographic techniques were used to present this large number of echo strengths in a single picture.

In the typical photographic presentation, an oscilloscope is operated so that the horizontal and vertical deflections correspond to scaled displacements of a reference map. The beam of this oscilloscope is then held on for a time proportional to the echo strength. This process is repeated until all areas of the map are filled in. The radar map is obtained by continuously photographing the face of the oscilloscope during this process. In this radar map, brightness is proportional to observed echo strength, and position is that of the reference map.

This photographic method of data presentation is extremely valuable for locating and identifying features with radar scattering differences. Also, numerical values for the scattering differences can be shown if display levels are quantized to specific levels. About nine intensity levels are possible in a photographic display, and these nine levels must represent scattering differences which may vary up to 2 orders of magnitude. Thus, the quantization was chosen as logarithmic increments which are spearated by a factor of 2 (see Table A-II of Appendix A). That is, the powers in each level are approxi-

mately twice the previous level and one-half of the next level. In comparison, typical statistical fluctuation of the echo is 10–15%.

In the quantization and presentation of the data, it is convenient to consider departures from the average. The average was computed by an iterative process so that obvious anomalies were not included. First, the average of echoes was computed for a map. In the succeeding iterations, echo strengths stronger than twice the previous average were not included in the average. The value of this average always converged by five steps. This average, of course, only applies to the area of a single observation: the area of an LAC chart.

This photographic presentation is shown in Plates A-I through A-XIX of Appendix A. To conserve space, two or more LAC charts are combined on a single plate. Maps with the same latitude range are shown together. In addition, special maps of Vallis Schroteri and Crater Posidonius are shown on Plate A-XIX. These two interesting areas fell at the conjunction of different LAC charts and were not adequately mapped in the other plates. Radar map projection is the same as for the LAC charts:

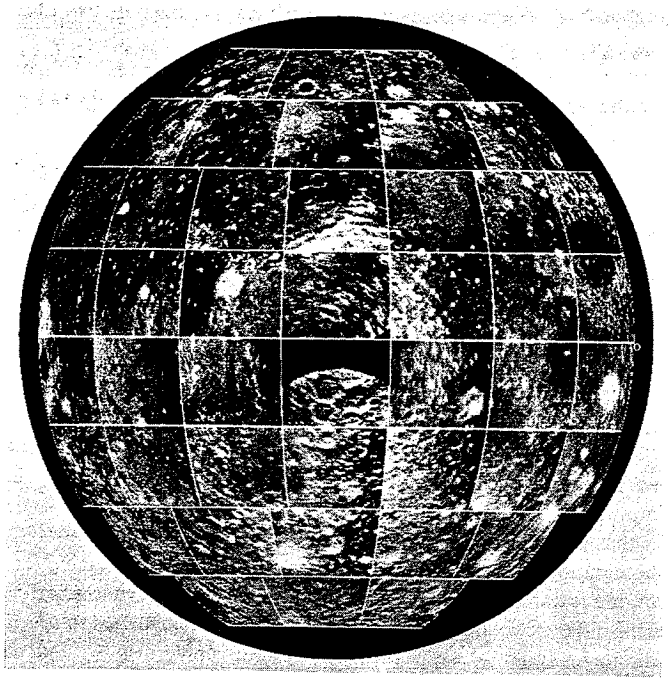

Fig. 1. A photomosaic of polarized lunar radar echoes at 70-cm wavelength. The Moon is shown at mean libration and individual radar maps are outlined. Radar echo strengths are normalized to show only departures from the average. Radar resolution was 25–100 km² on the surface.

the Mercator projection is used for equatorial regions and the Lambert conformal projection is used for nonequatorial regions.

In some maps, data processing errors can be identified. These errors, which are listed in Table A-III of Appendix A, are identified as follows:

(1) *Missing radar data.* In some cases, the sampling of the radar echoes in delay and/or frequency did not cover the entire mapped area. This typically occurred at the corners or edges of the map. A portion of the map for LAC 77 Purbach (Plate A-XI) is missing because the antenna beam had to be pointed to the south in order to adequately discriminate against echoes from conjugated reflecting ares.

(2) *Frequency smear.* Errors in the digital sampling of echoes tend to smear the echoes in frequency. Thus, echo power is erroneously redistributed into adjacent filters (but not redistributed in time delay). This tends to stretch the stronger echoes along circular paths about the subradar point.

(3) *Antenna cross-talk.* For radar echoes from areas near the subradar point, the extremely strong polarized echoes appear in the receiver assigned to depolarized echoes

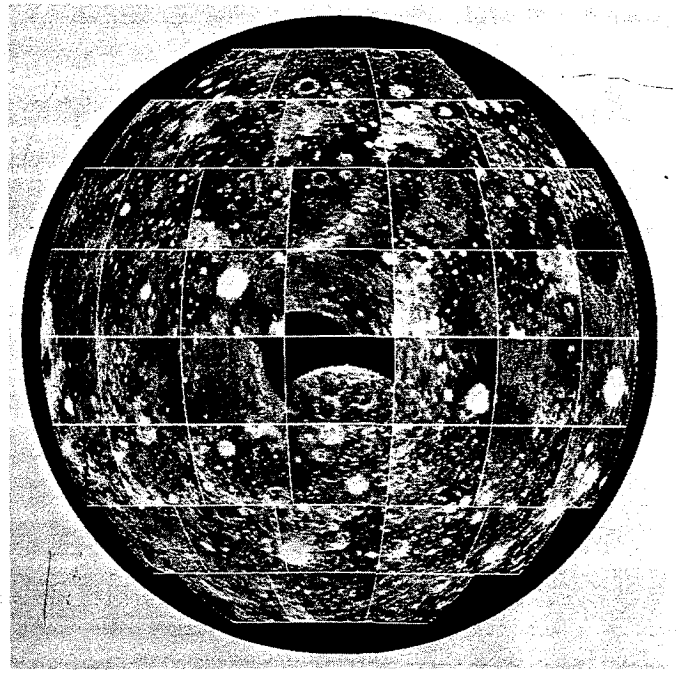

Fig. 2. A photomosaic of depolarized lunar radar echoes at 70-cm wavelength. The Moon is shown at mean libration and individual radar maps are outlined. Radar echo strengths are normalized to show only departures from the average. Radar resolution was 25–100 km² on the surface.

because of a very small amount of coupling between the two polarizations observed with the single antenna structure. On the two occasions when this was encountered, depolarized echoes were assigned the value indicating missing data.

In addition to plates described above, the radar echoes were collated into the photomosaics of Figures 1 and 2. These mosaics show the Moon at mean libration, and the brightness of the photograph indicates the departure of echo strength from the average. The smallest discernible differences in the mosaic show scattering differences of 10–20%, which are generally statistically significant. The brightest portions of the mosaics represent scattering differences of 5 times the average or greater. Scattering differences greater than 5 times the average are observed, but they saturate these displays.

Because of a fortuitous combination of projection and echo normalization, the depolarized radar map of Figure 2 shows the Moon as it would appear if one's eyes were sensitive to depolarized radar echoes. If one's eyes were sensitive to polarized echoes, then the Moon would appear with a very bright highlight at the center of the disk. Beyond this highlight, the Moon's disk would be slightly limb-dark. Both the highlight and the slight amount of limb darking were removed with the echo corrections mentioned above. Furthermore, the resolution of 25–100 km^2 for the radar maps of Figures 1 and 2 is equivalent to that of a medium-power optical telescope.

4. A Survey of Scattering Differences at 70-cm Wavelength

This section reviews the scattering differences presented in Figures 1 and 2 and the plates in Appendix A. Lists of radar features are given in Appendix B; only a brief discussion of this material is presented here.

The most outstanding features in the 70-cm radar maps are the large rayed craters: Tycho, Copernicus, Langrenus, Bullialdus, Theophilus, Kepler, and Aristarchus. Each of these craters has an enhancement of depolarized echoes of 10 to 15 times its environs. The polarized echoes are also enhanced, ranging from 3 times the average for Copernicus and Theophilus to about 10 times the average for Langrenus. These enhancements of polarized echoes are dependent upon the angle of incidence of the particular crater. Craters Copernicus and Theophilus near the subradar point and have small polarized echo enhancement. The other rayed craters are farther from the subradar point and have larger polarized echo enhancements. Also, the area of enhanced echoes extends beyond the crater by about one rim width in all directions as shown in Figure 3.

Besides these rayed craters, numerous other craters have enhanced echoes. Some young, nonrayed craters have enhancements as strong as those of the rayed craters. Generally, a crater with an enhancement of 70-cm radar echoes has a sharp rim and is surrounded by a hummocky ejecta pattern. In some cases, older craters such as Hevelius, Petavius and Gassendi, have definite 70-cm enhancements. Crater Gassendi, which has been partially flooded by mare material, is pre-mare in age.

Many of the craters having enhancements can be classified by their radar behavior or their optical appearance, as given in Tables B-I, B-II and B-III. Table B-I lists

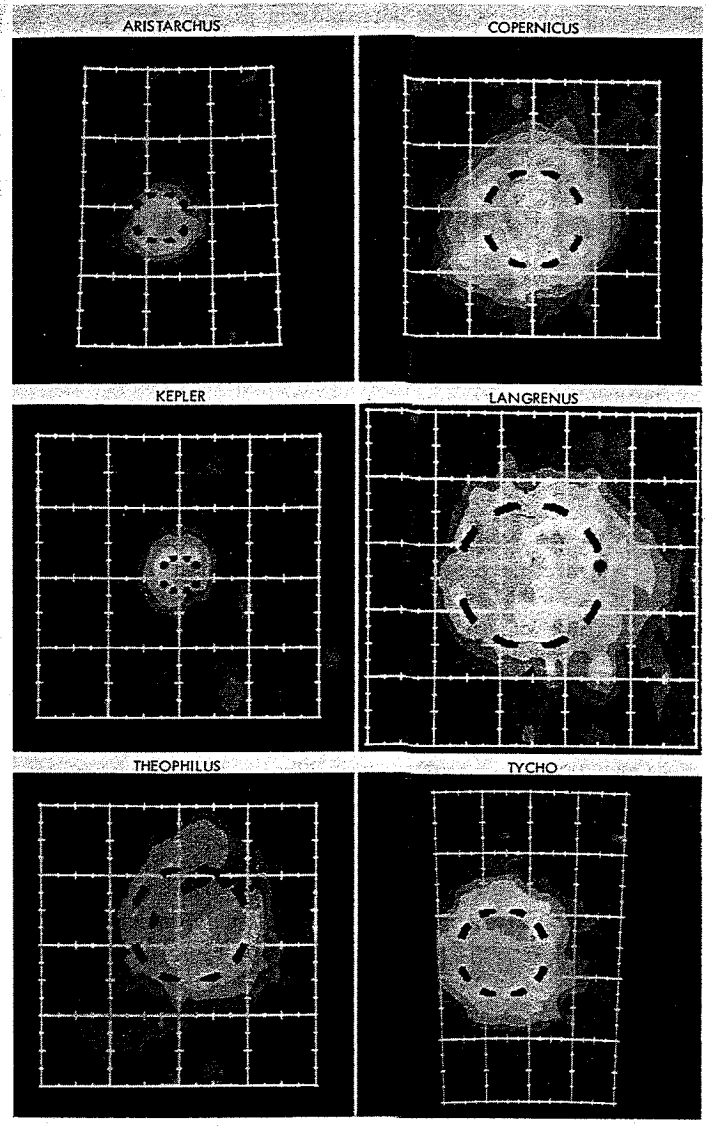

Fig. 3. Radar maps for the large rayed craters and their environs. Depolarized echoes are mapped. Shaded contours indicate backscatter power differences differeing by a multiplicative power of two Crater rims are outlined.

craters with a rim-bright appearance in the radar maps. For some cases, e.g., craters Plato and Archimedes, the floors of the craters have been flooded with mare material. Other rim-bright craters which have not been flooded are probably older (Eratosthenian) craters. For these older craters, the rims are still radar bright since mass wasting has continuously exposed rubble on the crater rims; the floors have weaker enhancements since the original rubble there has been covered with a regolith layer.

Table B-II lists craters which are surrounded by radar-dark haloes extending from about one-quarter to two crater radii beyond the radar-bright areas of crater floor and rim. Presumably, these radar-dark areas are blankets of ejecta with relatively few-meter-sized fragments, which mask the scattering of the pre-existing surface. Most of these dark haloes occur in maria near mare-highland contacts.

Table B-III lists 16 radar-bright craters with floors having large fracture patterns. One of these craters, Encke, has an unusual combination of infrared and radar characteristics (Thompson *et al.*, 1973).

A number of other features have distinct radar and morphological characteristics. Table B-IV lists the radar-bright mountain peaks and ridges that protrude from the maria. Many of these features are the inner rings of the Imbrium Basin. One of the features listed in Table B-IV is the Flamsteed Ring, which is probably the rim of a crater almost buried by mare material, The radar brightness indicates that this was one of the youngest of the pre-maria craters, a contemporary of Crater Gassendi mentioned above.

Table B-V lists rilles with detectable enhancements. One rille, Valli Schroteri, has a strong radar echo (see Plate A-XIX of Appendix A). Four rilles, Rima Sharp I, Rima Hadley, Rima Hyginus, and Rima Aristoteles I, had weaker (but detectable) enhancements. Rima Aristoteles I is a string of craters northwest of Crater Aristoteles. Rima Hadley is the target for Apollo 15; its radar and infrared characteristics are described in detail by Zisk *et al.* (1971). Other rilles could have enhancements, but the rilles are generally too small to be resolved with the 25–100 km^2 resolution of this mapping.

The features described thus far have enhanced radar echoes. However, there are

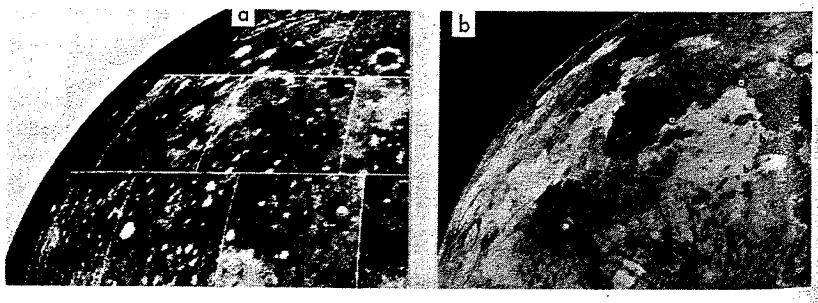

Fig. 4. Comparison of (a) radar scattering and (b) optical color differences for northern Mare Imbrium. Color differences taken from Figure 3.2 of Whitaker, 1965 (dark = red).

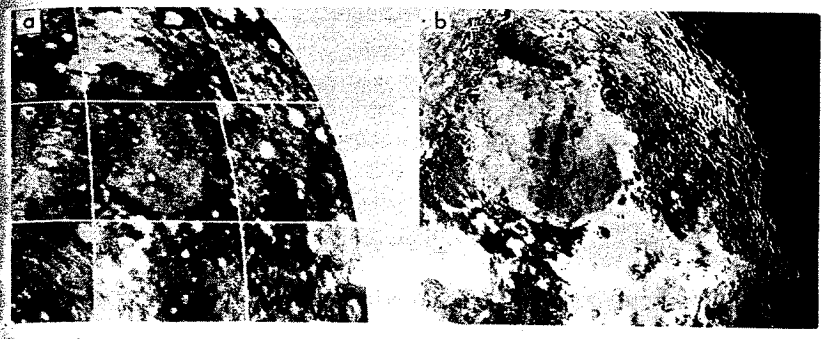

Fig. 5. Comparison of (a) radar scattering and (b) optical color differences for Mare Serenitatis and northern Mare Tranquilitatis. Color differences taken from Figure 3.1 of Whitaker, 1965 (dark = red).

other irregular areas (listed in Table B-VI) which have low radar echoes, dark albedoes, and low crater densities. Presumably these areas show very recent mantling.

Besides the features listed in Tables B-I through B-VI and described above, mare-highland contacts generally have a contrast in radar reflectivity. The highlands have the stronger echoes (by about a factor of 2). One notable exception is the dark halo which surrounds the Crater Plato, where the highlands have a lower reflectivity than the adjacent mare.

In addition to these mare-highland differences, the radar reflectivity varies across the same mare and possibly across the highlands. The most outstanding of the mare differences are the dark rim of Mare Serenitatis and the bright area in Mare Imbrium lying between the (bright-rim) Crater Plato and Crater Archimedes. Just west of the bright area in Mare Imbrium, there is an area of low radar reflectivity which is also the youngest mare unit in Mare Imbrium (Schaber *et al.*, 1970). In Mare Imbrum, these areas of different reflectivity have definite color differences, as shown in Figures 4 and 5. In the highlands, reflectivity differences are smaller and harder to distinguish. One area of lower reflectivity occurs in the eastern portion of the LAC quadrangle containing Tycho.

5. A Model for the Observed Scattering Differences

The scattering differences observed in the radar maps could arise from several causes such as tilts imposed by local topography, increased roughness on a wavelength (meter) scale, or an increased Fresnel reflection coefficient for specularly scattering surface. Manned and unmanned lunar exploration has shown that the lunar surface is comprised of dust interspersed with rock fragments. The radar results are difficult to interpret because the models for radio wave scattering of this type of surface are oversimplified and do not separate the rock backscatter from soil backscatter.

Even with these difficulties, a simple model can predict the relationship between the

polarized and depolarized enhancements for different types of lunar features. The basis of this model is the Moon's average behavior at meter wavelengths (as given, for example, by Hagfors; 1967; Table I). These radar measurements show that polarized echoes fall sharply as echoing areas are observed at larger angular distances from the subradar point. Radar observations were made by transmitting short pulses of energy and observing echo powers versus time delay. The earliest echoes come from the subradar point (the point on the Moon nearest the radar); the last echoes come from the limb region. For intermediate delays, the echoing area is observed at a mean angle of incidence θ given by

$$\theta = \arccos[1 - (\text{delay}/11.6\ \text{ms})].$$

This angle of incidence is the angle between the surface normal and the direction of the radar. Thus, this angle is zero at the subradar point and 90 deg at the limb.

There are significant differences between the observed polarized and depolarized echos. The polarized echo is strongest for the earliest echoes from the subradar point and then decreases sharply with increasing delay. Echo power has fallen by about 2 orders of magnitude when the angle of incidence is about 35 deg. Beyond the angle of incidence of 35 deg and up to about 80 deg, the average polarized echo falls at a gradual rate proportional to $(\cos\theta)^{1.5}$. Beyond the angle of incidence of 80 deg, the average echo power is proportional to $\cos(\theta)$. In contrast, the average depolarized echo is proportional to $\cos(\theta)$ for all angles of incidence and mimics the uniform brightness of the full Moon at visual wavelengths. However, the average polarized power at the limbs is still twice the average depolarized power.

This average echo behavior is interpreted by Evans and Hagfors (1964) as resulting from a quasi-specular and a diffuse component. The quasi-specular component arises from smooth facets which are many wavelengths across and pointed toward the radar. One notes that most of the lunar surface is observed at a glancing angle where a mirror reflection of incident radar energy is away from the radar. The diffuse component arises from surface roughness which spreads the reflected energy over all angles so that some of the reflected energy is directed back toward the radar. It is reasonable to assume that all of the depolarized echoes result from scattering by surface roughness. Polarized echoes from the limb are controlled by the diffuse component, while polarized echoes from the subradar point are controlled the quasi-specular component.

The question is whether the observed scattering differences can be interpreted in terms of the average scattering and the inferred quasi-specular and diffuse components. The effect of tilts can be predicted from average scattering alone. Areas such as crater walls or mountain sides which are tilted toward the radar are observed at smaller angles of incidence and have stronger echoes. This effect is greatest for polarized echoes near the subradar point. Also, strong angular dependence is seen for both the polarized and depolarized echoes from the limb. Echo enhancements from tilts occur in obvious places, but this effect cannot explain the strong echoes observed for floors of craters or other level areas.

Observed enhancements for areas have lower ratios polarized to depolarized power,

which suggest increases in the diffuse component of radar scattering. Increased surface roughness would be the major contributing factor. At this point in the discussion there is no reason to arbitrarily dismiss an increased quasi-specular component resulting from an increased Fresnel reflection coefficient. However, the average dielectric constant of the lunar soil is near 3, while the dielectric constant of rock is usually no larger than 25. Thus the quasi-specular component could not be expected to increase by 6, the ratio of the Fresnel reflection coefficients for dielectric constants of 3 and 25. This increase in the quasi-specular component is not enough to account for the larger observed enhancements.

In constructing a model for observed scattering differences, one must assume that both the quasi-specular and diffuse components can change. Also, the contribution of the diffuse component to polarized echoes must be defined. Here the radar observations can help. The large enhancements from the rayed craters have twice as much polarized power as depolarized power. This is the same ratio as average echoes at the limb, where the diffuse component dominates. This suggests that the diffuse component should vary as $\cos(\theta)$ for both the polarized echoes and depolarized echoes and should

Fig. 6. Panorama at Surveyor 7 landing site. This area has a depolarized radar enhancement of 10:1, but still appears to have many smooth areas. The largest rock in the foreground has a width of about 70 cm, the radar wavelength used for the measurements reported here. (Taken from mosaic 51, Bird et al., 1968.)

have a ratio of polarized to depolarized power of 2 for all angles of incidence. The quasi-specular component contributes only to polarized echoes and only to that portion of the polarized echoes not accounted for by the diffuse component.

With these arbitrary assignments of echo power to the diffuse and quasi-specular components, the increase in the diffuse component of the model must equal the depolarized enhancement. In other words, only the diffuse component can contribute to depolarized echoes. When the diffuse component of polarized echoes is increased by the depolarized enhancement, it accounts for all of the polarized enhancement within the experimental errors. Unfortunately, these experimental errors are fairly large, so this model was further modified to include changes in quasi-specular component. One could imagine an increase in the quasi-specular component if the floors of young craters were composed of fresh shock melted rocks and breccias which had not been ground to dust by meteoritic bombardment. Also, one could imagine a surface so rough that the flat facets would not exist and the quasi-specular scattering would disappear. The latter condition is unlikely in light of Surveyor 7 photographs.

The Surveyor 7 landing site lies in a 50-km^2 resolution cell which has a depolarized enhancement of 10 – about as strong as any depolarized enhancement of any level terrain on the Moon. But Surveyor 7 panoramas (see Figure 6) show that 90% or more of the terrain is a smooth, undulating surface which would contribute to the quasi-specular component. In light of these considerations, one should allow some variation in the quasi-specular component of this scattering model. In particular, this model allows the quasi-specular component to vary between a complete extinction to a times-two enhancement.

The simple mathematics for this model are given in Appendix C. The polarized enhancement predicted by this model is given by the ratio $(\alpha+\beta\pm\beta)/(1+\beta)$, where α is the observed depolarized enhancement and β is the ratio of the quasi-specular component to diffuse component of average polarized echoes at the angle of incidence of the feature. The largest value for β was 11.0 for Copernicus, which was observed at an angle of incidence of 22 deg. The smallest value of β was 1.0 for mare-highland differences observed at an angle of incidence of 60 deg.

Various predicted and observed scattering differences are listed in Table II. There is excellent agreement between the predicted polarized enhancement and that actually observed. This is true for both strong and weak enhancements and for the enhancements of large craters, mare-highland differences, and the rim floor differences of Plato and Archimedes. Craters with diameters smaller than 30 km were not included since their enhancements would include tilt effects. Unfortunately, the errors on the observations are too large to refine the change in quasi-specular component beyond the zero to times-two limits discussed above. However, changes beyond the times-two limit would have been detected.

In concluding this section, it should be mentioned that the model presented here is a modified version of one used for 3.8- and 70-cm radar enhancement from Tycho (Pettengill and Thompson, 1968). For the earlier work on Tycho, we concluded that $75\pm25\%$ of Tycho's floor was rough. If this earlier model were applied to the area of

TABLE II

Observed and predicted enhancements for lunar craters and mare-highland differences

Crater	LPL number[a]	θ = angle of incidence, (deg)	Observed depolarized enhancement	β = specular diffuse at angle θ	Predicted polarized enhancement	Observed polarized enhancement
Aristarchus	26470	49	13.0±3.0	1.8	5.3±1.7	7.5±2.0
Aristillus (17 Apr. 1968)	10515	41	6.2±1.0	2.1	2.7±1.0	3.2±0.6
Aristillus (25 Jan. 1967)	10515	40	5.2±0.7	2.1	2.4±0.9	2.6±0.4
Arzachel	30331A	21	3.5±1.0	12.8	1.2±1.0	1.5±0.5
Autolycus	10521	32	2.0±0.7	3.2	1.2±0.9	1.3±0.3
Bullialdus	33355	25	7.9±1.5	7.9	1.8±1.1	1.3±0.3
Campanus	34416	33	3.3±0.5	3.0	1.6±0.9	1.5±0.5
Cavalerius (19 Feb. 1969)	29018	60	8.0±2.0	1.4	3.9±1.4	5.5±1.0
Cavalerius (3 Jul. 1969)	29018	64	8.5±1.0	1.2	4.4±1.0	6.0±1.0
Copernicus (2 Dec. 1968)	23136A	28	11.0±2.0	5.1	2.8±1.3	3.0±0.5
Copernicus (21 Sept. 1967)	23136A	22	10.0±2.0	11.0	1.8±1.1	2.0±0.5
Eudoxus	12609	54	7.2±2.0	1.6	3.4±1.4	3.3±0.8
Hevelius	29023	60	5.0±1.0	1.4	2.7±1.0	3.0±0.5
Hevelius	29023	64	5.0±1.0	1.2	2.8±1.0	3.5±0.5
Kepler	26104	32	10.0±1.0	3.2	3.1±1.0	2.5±0.5
Langrenus (18 Feb. 1967)	48165	68	11.5±1.5	1.0	6.2±1.2	3.5±0.4
Langrenus (3 Jul. 1967)	48165	64	11.0±2.0	1.2	5.5±1.4	5.0±1.0
Sirsalis/Sirsalis A	38241/38252	55	7.0±1.5	1.6	3.3±1.2	4.0±1.0
Taruntius	17029	52	2.5±0.5	1.7	1.6±0.8	1.5±0.3
Theophilus	44139	34	5.0±1.0	2.8	2.0±1.0	2.5±1.0
Tycho	31648A	36	15.0±2.0	2.6	4.9±1.3	5.0±0.1
Werner	40457	31	5.8±1.0	3.2	2.1±1.0	2.5±1.0
Crater rim/floor differences						
Archimedes	20469	30	2.5±0.5	4.6	1.3±0.9	1.3±0.3
Plato	20798	58	6.0±2.0	1.5	3.0±1.4	2.5±0.5
Maria-highlands differences						
Montes Caucasus/Mare Serenitatis		43	4.0±1.0	2.0	2.0±1.0	2.0±0.5
Montes Taurus/Mare Serenitatis		45	2.8±0.5	1.9	1.6±0.8	2.3±0.5
Highlands/Mare Crisium		66	3.0±0.5	1.0	2.0±0.8	2.0±0.5
Highlands/Mare Fecunditatis		61	2.0±0.5	1.3	1.9±0.8	1.07±0.5
Highlands/floor of Grimaldi		62	5.0±1.0	1.2	2.8±1.0	2.5±0.5

[a] See Arthur *et al.* (1963, 1964, 1965 and1966) for crater position and diameter.

the Surveyor 7 landing site, we would have concluded that $50 \pm 25\%$ of the Surveyor 7 site would be covered with meter-sized roughness. This, of course, predicts more rocks than are observed in the Surveyor 7 photographs. With the present model, the conclusion is that Tycho's floor has 15 times more rough elements than the average surface. Similarly, the Surveyor 7 landing site has 10 times more rough elements than the average surface. It is expected that these rough elements are angular rocks of wavelength (meter) size. This is borne out by the Surveyor rock counts. Furthermore, it should be noted again that the errors in the measurement allow for a 2:1 increase in the quasi-specular component and that this increase is equivalent to increasing the dielectric constant from 2.7 to 4.0. However, further increases in the dielectric constant or the quasi-specular power are not consistent with this model.

6. Concluding Remarks

This radar mapping of the lunar surface has yielded information about lunar surface conditions on a meter scale with a real resolutions of 25–100 km^2. For lunar studies, this information complements the mapping of the Moon at the shorter wavelength of 3.8 cm to be described in the next paper in this series. These two radar mappings, along with the infrared eclipse measurements, can specify lunar surface conditions on centimeter-to-meter scale for the earth-facing hemisphere of the Moon (Thompson *et al.*, 1973; and Zisk *et al.*, 1971). For a much smaller portion of the lunar surface, surface conditions of this scale have been observed only at the Surveyor landing sites and at the past and future Apollo landing sites. With this 'ground-truth' data, the remote sensing data is invaluable in predicting surface conditions elsewhere on the Moon.

Appendix A

Photographic Presentation of 70-cm Radar Maps of the Moon

In this appendix the LAC chart radar maps are given in Plates A-I through A-XVIII, as listed in Table A-I. Plate A-XIX shows Vallis Schroteri and Crater Posidonius. The radar map projection is that of the LAC charts; the Mercator projection is used for the equatorial region and the Lambert conformal projection is used for the non-equatorial regions. Grid lines on the radar maps are given every 2 deg, and tick marks are given every $\frac{1}{2}$ deg. The radar maps are quantized to the levels given in Table A-II. A change in level corresponds to a change in echo power by a multiplicative factor of 2. Errors in data processing are listed in Table A-III.

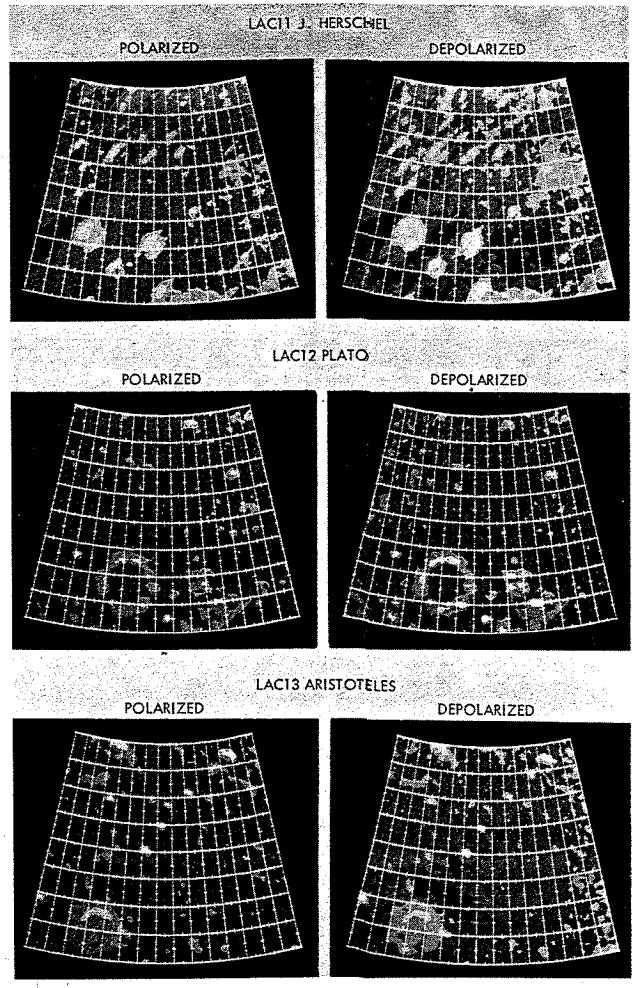

Plate A-I. Radar maps, LAC 11, 12, 13.

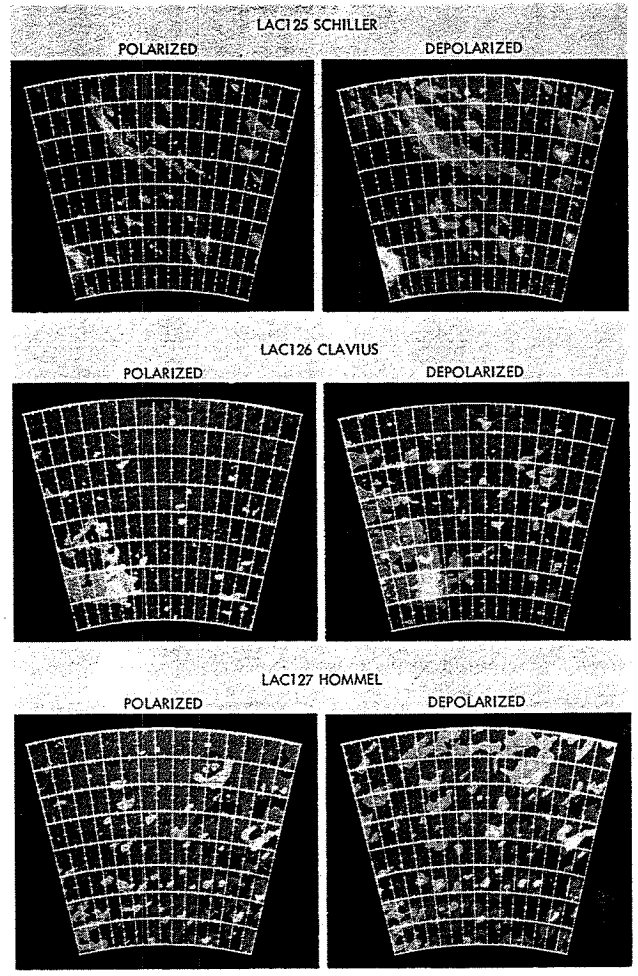

Plate A-XVIII. Radar maps, LAC 125, 126, 127.

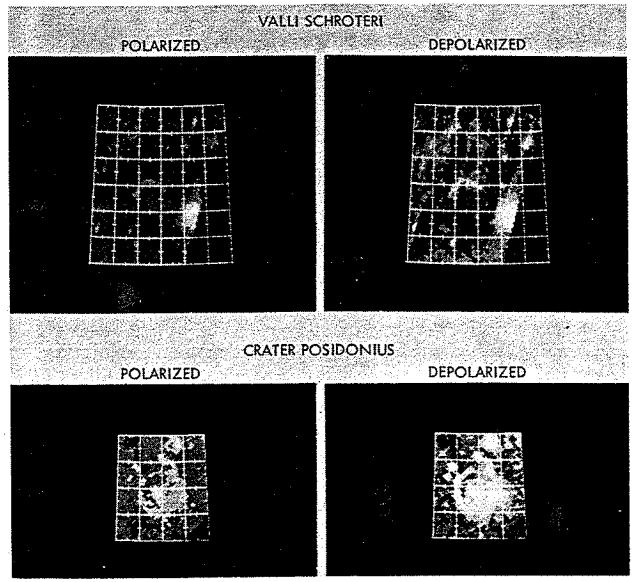

Plate A-XIX. Radar maps, Vallis Schroteri, Crater Posidonius.

Appendix B

List of Lunar Features with Unusual Radar Properties

As may be seen from Figures 1 and 2, a very large number of lunar craters show a radar scattering enhancement, particularly in the depolarized mode, as compared to their surroundings. Certain of these are particularly remarkable, and these have been listed in Tables B-I through B-III, using the format of the Lunar and Planetary Laboratory Catalog (Arthur *et al.*, 1963, 1964, 1965 and 1966). Since all the craters listed are nearly circular, the entry for the minor diameter is zero. The following code specifies the crater environs:

C = highlands
AM = pre-maria
PM = post-maria
PMC = maria-highlands border (crater is post-maria)
AMC = maria-highlands border (crater is pre-maria).

Table B-IV lists ridges and peaks with enhanced radar echoes; Table B-V lists rilles with radar enhancements; and Table B-VI lists lunar areas with low echoes and the appearance of recent mantling.

TABLE B-I

Craters with distinct radar enhancements from their rims

LPL number	Blagg Muller number	Crater name	Long (deg)	Lat (deg)	Major diam. (km)	Minor diam. (km)	Crater class	Crater background	LAC chart
20798	1062	Plato	−9.2	51.4	100.0	0.0	2F	C	12
11796	710	Aristoteles	17.3	50.1	87.3	0.0	2	C	13
12609	726	Eudoxus	16.3	44.2	67.1	0.0	1	C	26
20469	1144	Archimedes	−4.0	29.7	82.6	0.0	2F	AMC	41
34416	2525	Campanus	−27.7	−28.0	48.0	0.0	2	PMC	94
32409	2784	Pitatus	−13.5	−29.8	104.8	0.0	3	AMC	94
41596	3819	Gem. Fris.	13.4	−34.3	87.7	0.0	3	C	113
41686A	3846	Maurolycus	14.0	−41.8	114.2	0.0	3	C	113

TABLE B-II

Craters surrounded by a halo of distinctly low radar echoes

LPL number	Blagg-Muller number	Crater name	Long (deg)	Lat (deg)	Major diam. (km)	Minor diam. (km)	Crater class	Crater background	LAC chart
20798	1062	Plato	−9.2	51.4	100.0	0.0	2F	C	12
20755	1075	Plato J	−4.5	48.9	7.7	0.0	1	C	12
11796	710	Aristoteles	17.3	50.1	87.3	0.0	2	PM	13
10515	917	Aristillus	1.2	33.8	55.3	0.0	1	PM	25
26470	1755	Aristarchus	−47.6	23.7	45.3	0.0	1	PMC	39
28178	1843	Galilaei	−62.7	10.5	15.5	0.0	1	PM	56
28270	1844	Galilaei A	−62.9	11.7	11.2	0.0	1	PM	56
28112	1832	Reiner	−54.9	6.9	29.9	0.0	1	PM	56
44139	4195	Theophilus	26.3	−11.4	100.0	0.0	2	PMC	78
33355	2813	Bullialdus	−22.2	−20.7	58.9	0.0	1	PM	94

TABLE B-III

Craters with enhanced 70-cm radar echoes and fracture patterns on the floors

LPL number	Blagg-Muller number	Crater name	Long (deg)	Lat (deg)	Major diam. (km)	Minor diam. (km)	Crater class	Crater background	LAC chart
14782	437	Atlas	44.4	46.6	87.4	0.0	2	C	27
15672	374	Franklin	47.6	38.8	56.3	0.0	2	C	27
15548	383	Maury A	41.9	36.0	21.0	0.0	2F	PMC	27
28434	1859	Briggs	−68.8	26.4	38.6	0.0	2	PM	38
29023	1944	Hevelius	−67.5	2.2	117.9	0.0	3	PMC	56
25097	1538	Encke	−36.6	4.6	29.4	0.0	2	AMC	57
17029	215	Taruntius	46.5	5.6	55.9	0.0	2F	PMC	61
37179	2117	Hansteen	−51.9	−11.5	44.8	0.0	3	AMC	74
38440	2051	Byrgius D	−67.3	−24.1	25.8	0.0	1	C	92
36310	2389	Gassendi	−39.8	−17.5	110.4	0.0	3	AMC	93
37306	2147	Mersenius	−49.2	−21.5	81.5	0.0	2F	C	93
35520	2353	Vitello	−37.5	−30.4	44.6	0.0	2	C	93
30367	3070	Thebit	−4.0	−22.0	54.7	0.0	2	C	95
30331A	3040	Arzachel	−1.9	−18.2	96.8	0.0	2	C	95
46217	4357	Buhnenberger	40.1	−16.2	33.0	0.0	2	PM	97
47482	4636	Petavius	60.4	−25.3	176.6	0.0	2	C	98

TABLE B-IV

Ridges and isolated mountain peaks which had enhanced 70-cm radar echoes

Mountain	Longitude	Latitude	LAC chart
Montes Teneriffe ε	−14°40′	48°50′	12
Montes Teneriffe α, δ, κ, γ, ι	−13°00′	47°30′	25
Pico	−8°40′	45°50′	25
Pico β	−8°20′	43°30′	25
Monte Spitzbergenis μ	−5°30′	36°40′	25
Montes Spitzbergensis α, β, γ, ε, κ, θ	−5°00′	35°00′	25
Piton	−0°50′	40°40′	25
Unnamed peak in Montes Harbinger	−41°00′	28°00′	39
La Hire	−25°30′	27°40′	40
Flamsteed Ring	−44°00′	−3°00′	75

TABLE B-V

Rilles with 70-cm radar enhancements

Rille	Longitude	Latitude	LAC chart
Rima Aristoteles I (string of craters in LO IV Frame 104)	15° 30′	53° 54°	13
Rima Sharpi	50°30′	46°, 48°	23
Vallis Schröteri	−53°, −49°	24°, 26°	38
Rima Hadley	2°, 3°	25°, 26°	41
Rima Hyginus	6°, 9°	7°, 8°	59

TABLE B-VI

Lunar areas with low 70-cm radar echoes and appearance of recent mantling in Orbiter photographs

Area	Longitude	Latitude	LAC chart
In Mare Frigoris northeast of Montes Alpes	2°, 4°	52°, 53°	12
On northwest shore of Lacus Somniorum	21°, 22°	40°30′, 41°30′	26
West of Mare Humorum	−50°, −48°	−25°, −26°	93
Western shore of Mare Humorum	−45°, −44°	−26°, −26°	93
Between Vieta T and La Croix K	−59°, −57°	−39°, −33°	110
Floor of Drebbel E	−52°, −50°	−39°, −37°	110
Flow that meanders northeast from Drebbel E	−49°, −46°	−39°, −36°	110
Northern floor of Schickard	−58°, −52°	−44°, −41°	110
Southeast floor of Schickard	−53°, −51°	−47°, −44°	110
Flooded plain southwest of Schiller	−46°, −42°	−56°, −53°	125

Appendix C

Enhancement Predictions for a Quasi-Specular, Diffuse Model of Lunar Radar Scattering

This appendix gives the simple mathematics of the model which was used in Section 5 for predicting radar enhancements from the quasi-specular and diffuse components of lunar scattering.

It is assumed that the quasi-specular and diffuse contributions to the average echo are

$$P_{\text{ave}} = P_d + P_q \tag{C-1}$$

$$D_{\text{ave}} = D_d = \tfrac{1}{2}P_d \tag{C-2}$$

where

P_{ave} = average backscattered polarized power
D_{ave} = average backscattered depolarized power
P_d = diffuse contribution to the polarized power
D_d = diffuse contribution to the depolarized power
P_q = quasi-specular contribution to the polarized power.

There is no quasi-specular contribution to the depolarized echo power.

To account for an enhancement, the diffuse component has to increase by an amount α equal to the depolarized enhancement. The quasi-specular component can vary between a total extinction ($P_q=0$) to a times-two increase ($P_q=2P_q$). Thus, at the enhanced area, the polarized and depolarized powers, P_e and D_e, are

$$P_e = \alpha P_d + (1 \pm 1)P_q \tag{C-3}$$

$$D_e = \alpha D_d. \tag{C-4}$$

The depolarized enhancement is simply α. The polarized enhancement is:
Let $P_q/P_d=\beta$; then

$$P_e/P_{\text{ave}} = \frac{\alpha P_d + (1 \pm 1)\, P_q}{P_d + P_q} \tag{C-5}$$

$$P_e/P_{\text{ave}} = \frac{\alpha + (1 \pm 1)\, \beta}{(1+\beta)} = \frac{\alpha + \beta \pm \beta}{1+\beta}. \tag{C-6}$$

References

Arthur, D. W. G. *et al.*: 1963, *Communications of the Lunar and Planetary Laboratory*, 2, No. 30, pp. 71–78.
Arthur, D. W. G. *et al.*: 1964, *Communications of the Lunar and Planetary Laboratory*, 3, No. 40, pp. 1–2.
Arthur, D. W. G. *et al.*: 1965, *Communications of the Lunar and Planetary Laboratory*, 4, No. 50, pp. 61–62.

Arthur, D. W. G. *et al.*: 1966, *Communications of the Lunar and Planetary Laboratory*, 3, No. 70, pp. 1–2.
Evans, J. V. and Hagfors, T.: 1964, *Icarus* **3**, 151–160.
Hagfors, T.: 1967, *Radio Sci.* **2** (new series), 445–465.
Pettengill, G. H. and Thompson, T. W.: 1968, *Icarus* **8**, 3, 457–471.
Schaber, G. G., Eggleton, R. E., and Thompson, T. W.: 1970, *Nature* **226**, 1236–1239.
Thompson, T. W., Masursky, H., Shorthill, R. W., Tyler, G. H., and Zisk, S. H.: 1973, *The Moon*, this issue, p. 87.
Thompson, T. W. and Dyce, R. B.: 1965, *J. Geophys. Res.* **71**, 4843–4853.
Whitaker, E. A.: 1965, in W. N. Hess, D. H. Menzel, and J. A. O'Keefe (eds.), *The Nature of the Lunar Surface*, Proceedings of the 1965 IAU-NASA Symposium, pp. 79–93.
Zisk, S. H., Carr, M. H., Masursky, H., Shorthill, R. W., and Thompson, T. W.: 1971, *Science* **173**, 808–811.